

Article

# Steering Stability Control for a Four Hub-Motor Independent-Drive Electric Vehicle with Varying Adhesion Coefficient

Rufei Hou <sup>1,2</sup> , Li Zhai <sup>1,2,\*</sup>  and Tianmin Sun <sup>3</sup>

<sup>1</sup> National Engineering Laboratory for Electric Vehicles, Beijing Institute of Technology, Beijing 100081, China; 2120170337@bit.edu.cn

<sup>2</sup> Co-Innovation Center of Electric Vehicles in Beijing, Beijing Institute of Technology, Beijing 100081, China

<sup>3</sup> BAIC BJEV Inc., Beijing 100021, China; suntianmin@bjev.com.cn

\* Correspondence: zhaili26@bit.edu.cn; Tel.: +86-10-6891-5202

Received: 30 August 2018; Accepted: 11 September 2018; Published: 14 September 2018



**Abstract:** In order to enhance the steering stability of a four hub-motor independent-drive electric vehicle (4MIDEV) on a road with varying adhesion coefficient, for example on a joint road, this paper proposes a hierarchical steering stability control strategy adapted to the road adhesion. The upper control level of the proposed strategy realizes the integrated control of the sideslip angle and yaw rate in the direct yaw moment control (DYC), where the influences of the road adhesion and sideslip angle are both studied by the fuzzy control. The lower control level employs a weight-based optimal torque distribution algorithm in which weight factors for each motor torque are designed to accommodate different adhesion of each wheel. The proposed stability control strategy was validated in a co-simulation of the Carsim and Matlab/Simulink platforms. The results of double-lane-change maneuver simulations under different conditions indicate that the proposed strategy can effectively achieve robustness to changes in the adhesion coefficient and improve the steering stability of the 4MIDEV.

**Keywords:** electric vehicles; independent-drive; steering stability; adhesion coefficient

## 1. Introduction

With the rapid development of motor technology, the four hub-motor independent-drive electric vehicle (4MIDEV) concept has emerged [1,2]. Different from the traditional centralized drive vehicle, the 4MIDEV is directly driven by four hub motors without the need for clutches, drive shafts and other mechanical components. The drive/brake torque of four hub motors not only responds quickly and accurately, but also can be independently controlled, which helps a lot to improve the stability and maneuverability of the vehicles [3]. Since traditional electronic stability program (ESP) cannot be directly applied to the 4MIDEV, its steering stability control has attracted much attention from researchers [4–7].

The stability control strategy with hierarchical structure for the 4MIDEV has been widely used and proved to be effective, including an upper control level to generate the yaw moment command, and a lower control level to change the yaw moment to the torque required for four drive wheels [5–8]. However, few studies have enabled the stability control strategy to adapt to the adhesion coefficient, but only focus on the constraints of road adhesion. Furthermore, relevant verifications are always neglected when the adhesion coefficient changes, which may bring more control errors and adversely affect the final steering stability control effect. As the driving conditions of vehicles become more complex, it is necessary to study a stability control strategy adaptive to road adhesion to ensure good

steering stability of the 4MIDEV, which puts forward higher requirements for the upper control level and the lower control level.

In general, the upper control level is usually designed based on the direct yaw moment control (DYC) which controls the lateral motion of vehicle through a yaw moment. The sideslip angle and yaw rate corresponding to stability and maneuverability are always selected as the control targets in the DYC [9–12]. However, unlike the yaw rate, there is no direct relationship between the sideslip angle and the yaw moment, but they are related to each other by nonlinear tire forces. Most of the DYCs previously proposed only control the yaw rate and ignore the impact of the sideslip angle. For example, Tahami et al. [13] and Lin et al. [14] adopted fuzzy control and sliding mode control, respectively, in the DYC, and both successfully realized the control of the yaw rate without the consideration of the sideslip angle. However, the importance of the sideslip-angle control is much greater than that of the yaw-rate control when the adhesion coefficient is low. The lack of consideration for the sideslip angle will be detrimental to the steering stability control effect, especially when the road adhesion coefficient changes. Some studies have improved the DYCs on the basis of the previous ones in which the sideslip angle was only taken as an intermediate variable in the control of the yaw rate, and finally achieved good results. Zou et al. [15] and Tahami et al. [16] redesigned the reference yaw rate based on the sideslip angle respectively, and both finally achieved a good control of the sideslip angle and the yaw rate by tracking the yaw rate with the reference value. Zhai et al. [17] weighted the sideslip angle and the yaw rate to obtain a comprehensive control quantity and also achieved good control performance. Although the above methods have basically considered the influence of the sideslip angle, the impact of adhesion coefficient was neglected, and there was a lack of correlation verification when the adhesion coefficient changes. With different adhesion coefficients, the effects of the sideslip angle and the yaw rate on the stability are quite different. Therefore, a new DYC adapted to road adhesion is required to achieve the integrated control of sideslip angle and yaw rate.

The torque distribution algorithm is a key part in the lower control level. The optimal distribution algorithm has been widely adopted and proved to be effective compared with other torque distribution algorithms such as average distribution [18], etc., which makes the allocation to meet optimal objectives as much as possible. In current studies, the tire workload usage is always selected as the main optimal objective to reflect steering stability. Jin et al. [19] and Park et al. [20] developed an optimal distribution algorithm based on the tire workload usage objective respectively, and the steering stability of the vehicle was improved. In [21], Zhai et al. designed an energy consumption objective in addition to tire workload usage objective, and finally achieved energy savings while ensuring stability through multi-objective optimization. Furthermore, Li et al. [22] additionally considered the control objective and ensured the accuracy of stability control. These methods have been proven to be effective in the face of the road with constant adhesion coefficient, but they did not consider the influence of changes in adhesion coefficient. For the stability control, the workload usage of each tire was generally considered equally important to each other, i.e., different adhesion conditions at each wheel were ignored, which may result in a wheel with low adhesion experiencing extreme loads while other wheels maintain a relatively high stability margin.

To solve the above problems, this paper proposes a hierarchical stability control strategy that is adaptive to the road adhesion coefficient. The upper control level of the proposed strategy realizes the integrated control of the sideslip angle and yaw rate in which the influences of the sideslip angle and road adhesion are both studied by the fuzzy control. As the road adhesion coefficient is also taken into account in the yaw moment control, the output of the DYC becomes more reasonable. The lower control level employs a weight-based optimal distribution algorithm in which weight factors for each tire workload usage are designed to accommodate different adhesion of each wheel. The different weight control of each wheel torque allows the 4MIDEV to better adapt to changes in adhesion coefficient.

The rest of this study is organized as follows: in Section 2, the 4MIDEV system model, including the vehicle dynamics model, driver model, etc., is presented. The proposed hierarchical strategy for the 4MIDEV is then designed in Section 3. In Section 4, the proposed strategy is evaluated by

a co-simulation using CarSim and Matlab/Simulink under different double-lane-change maneuver conditions. Finally, the conclusions are summarized in Section 5.

## 2. System Overview and Modeling

The 4MIDEV, as shown in Figure 1, is directly driven by four hub motors without the need for clutches, drive shafts and other mechanical components. The drive/brake torque of four hub motors can be independently controlled by a main electronic controller using the CAN bus (a kind of area network), according to the driver’s operation and actual vehicle condition.

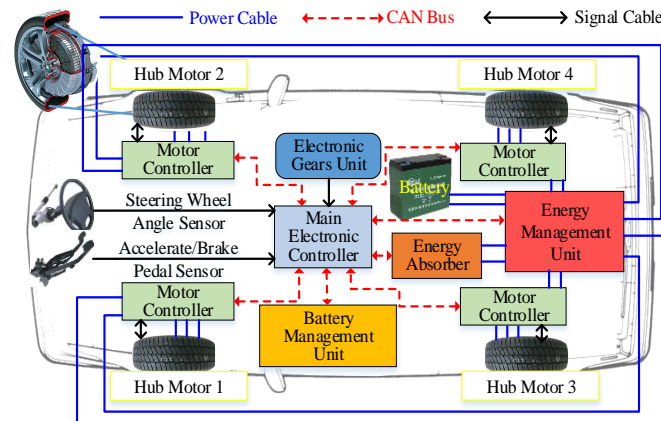


Figure 1. System Configuration of the 4MIDEV.

### 2.1. Vehicle Dynamics Model

Ignoring the pitch and roll motions, a simplified three-degree-of-freedom (3-DOF) dynamic model is elaborated to study the vehicle’s planar motion: yaw motion, longitudinal motion, and lateral motion, as shown in Figure 2a, where  $\dot{V}_x$  and  $\dot{V}_y$  denote the derivative of the longitudinal velocity  $V_x$  and the lateral velocity  $V_y$ , respectively,  $\dot{\gamma}$  is the derivative of the yaw rate  $\gamma$ .  $m$  denotes the mass of the vehicle,  $I_z$  is the yaw inertia of the vehicle.  $F_{xij}$  and  $F_{yij}$  denote the longitudinal and lateral forces of the respective wheels, respectively, where  $i \in \{f, r\}$  denotes the front or the rear and  $j \in \{l, r\}$  denotes the left or the right.  $\delta_f$  denotes the front wheel steering angle.  $a$  and  $b$  are the distance between the center of gravity and the front axle and rear axle, respectively.  $d$  is half of the tread.

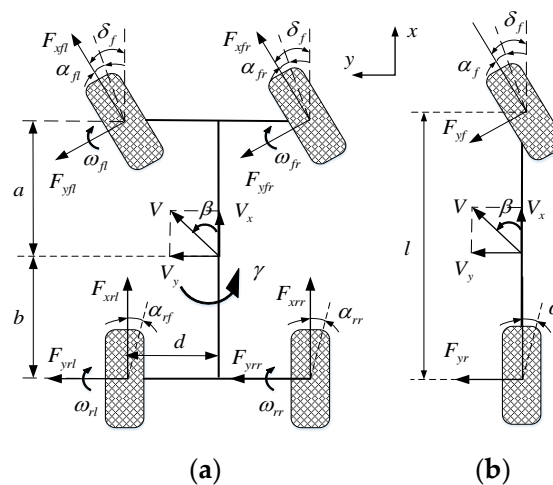


Figure 2. Dynamic models of the 4MIDEV. (a) 3-DOF model. (b) 2-DOF model.

The dynamic equations of the 3-DOF model can be expressed in matrix form as:

$$\begin{bmatrix} \dot{V}_x \\ \dot{V}_y \\ \dot{\gamma} \end{bmatrix} = \begin{bmatrix} V_y \gamma \\ -V_x \gamma \\ 0 \end{bmatrix} + \mathbf{B}_x \begin{bmatrix} F_{xfl} \\ F_{xfr} \\ F_{xrl} \\ F_{xrr} \end{bmatrix} + \mathbf{B}_y \begin{bmatrix} F_{yfl} \\ F_{yfr} \\ F_{yrl} \\ F_{yrr} \end{bmatrix} \quad (1)$$

where the coefficient matrices  $\mathbf{B}_x$  and  $\mathbf{B}_y$  are:

$$\mathbf{B}_x = \begin{bmatrix} \frac{\cos \delta_f}{m} & \frac{\cos \delta_f}{m} & \frac{1}{m} & \frac{1}{m} \\ \frac{\sin \delta_f}{m} & \frac{\sin \delta_f}{m} & 0 & 0 \\ \frac{a \sin \delta_f - d \cos \delta_f}{I_z} & \frac{a \sin \delta_f + d \cos \delta_f}{I_z} & -\frac{d}{I_z} & \frac{d}{I_z} \end{bmatrix} \quad (2)$$

$$\mathbf{B}_y = \begin{bmatrix} -\frac{\sin \delta_f}{m} & -\frac{\sin \delta_f}{m} & 0 & 0 \\ \frac{\cos \delta_f}{m} & \frac{\cos \delta_f}{m} & \frac{1}{m} & \frac{1}{m} \\ \frac{a \cos \delta_f + d \sin \delta_f}{I_z} & \frac{a \cos \delta_f - d \sin \delta_f}{I_z} & -\frac{b}{I_z} & \frac{b}{I_z} \end{bmatrix} \quad (3)$$

## 2.2. Tire Model

The tire model reflects the nonlinear characteristics of tire dynamics, which is a critical part for steering stability control. The ‘‘Magic Formula’’ tire model [23] and ‘‘Unified Index’’ tire model [24] have been widely used and proven to be effective, but too much characteristic parameters of the tire are required. In order to improve the real-time performance of the system, a simplified tire model in [21] is used as follows:

$$F_{yij} = -K_{\alpha ij} \sqrt{1 - \left( \frac{F_{xij}}{\mu_{ij} F_{zij}} \right)^2} \frac{\mu_{ij}}{k} \tan^{-1} \left( \frac{k}{\mu_{ij}} \alpha_{ij} \right) \quad (4)$$

$$k = \frac{K_{\alpha ij} \pi}{2 F_{zij}}$$

where  $\mu_{ij}$  denotes the road adhesion coefficient,  $K_{\alpha ij}$  and  $\alpha_{ij}$  denote the lateral stiffness and slip angle of each tire, respectively.

## 2.3. Hub Motor Model

The hub motors typically employ a permanent magnet synchronous motor (PMSM) that can be modeled using a space vector control method. Considering that the torque dynamic response of the PMSM is much faster than the vehicle dynamic response, the dynamic response of the motor can be simplified to a second-order system whose torque transfer function can be expressed as:

$$G(s) = \frac{T_{ij}}{T_{ij}^*} = \frac{1}{2\tau^2 s^2 + 2\tau s + 1} \quad (5)$$

where  $\tau$  denotes the damping ratio, and its value is initially set to 0.01.  $T_{ij}^*$  denotes the motor drive torque command, and  $T_{ij}$  is the actual drive torque.

## 2.4. Driver Model

A ‘‘preview-follow’’ driver model [25] is adopted in this paper to simulate the driver’s operations on the acceleration/brake pedal and steering wheel based on the desired vehicle speed and the expected route. The driver’s preview time is set to 1 s for the closed-loop test. Then the front-wheel-steer angle can be obtained.

### 3. Design of Hierarchical Steering Stability Control Strategy for the 4MIDEV

In this paper, the stability control strategy proposed for the 4MIDEV is designed as a hierarchical structure, including a reference output level, an upper control level with the yaw moment control, and a lower control level based on the torque allocation, as shown in Figure 3. A reference dynamic model is established in the reference output level to obtain the desired vehicle dynamics parameters. The upper control level is composed of speed control and yaw moment control to realize adaptive control of the vehicle speed, yaw rate, and sideslip angle, respectively. The lower control level optimally distributes the virtual control forces generated by the upper control level, such as the yaw moment, to each hub-motor controller in the form of the driving/brake torque commands, so as to realize the steering stability control of the 4MIDEV.

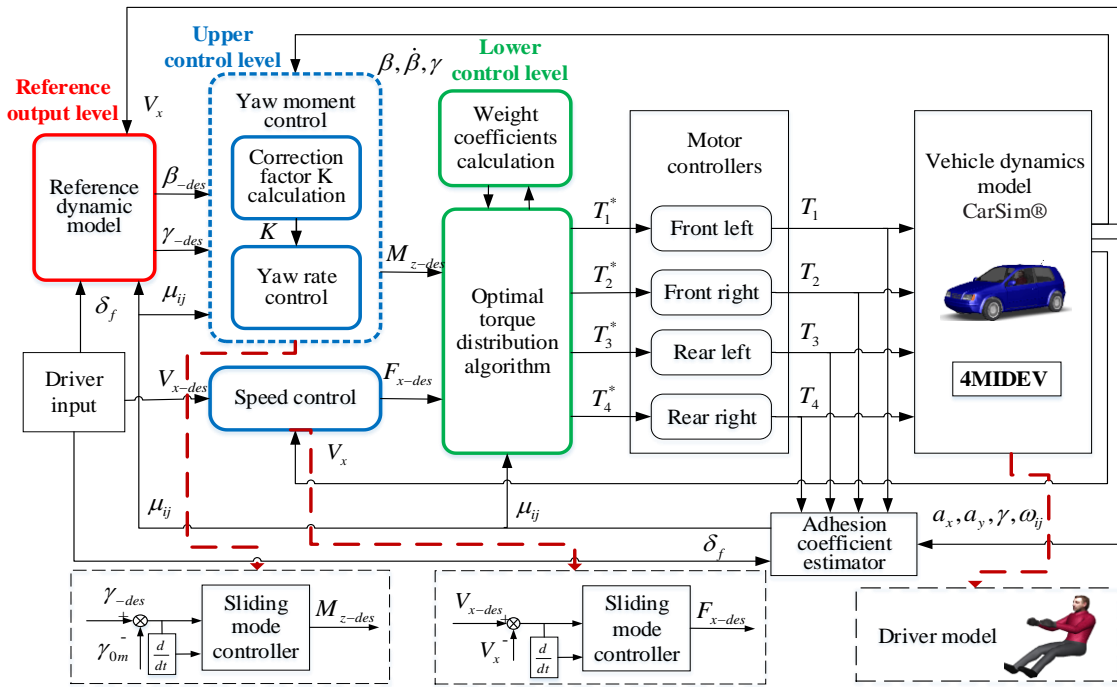


Figure 3. The configuration of hierarchical stability control strategy.

#### 3.1. Reference Output Level

To directly and clearly reflect the driver’s steering intention, the reference output level simplifies the above 3-DOF model to 2 DOFs as the reference dynamics model, as shown in Figure 2b, which makes the steady-state responses of the vehicle linear with the driver input. The kinetic equations can be formulated as follows:

$$\begin{cases} mV_x(\dot{\beta} + \dot{\gamma}) = F_{yf} \cos \delta_f + F_{yr} \\ I_z \dot{\gamma} = aF_{yf} \cos \delta_f - bF_{yr} \end{cases} \quad (6)$$

where  $\dot{\gamma}$  and  $\dot{\beta}$  are the derivative of the yaw rate  $\gamma$  and the sideslip angle  $\beta$ , respectively.  $F_{yf}$  and  $F_{yr}$  denote the lateral tire force of the front and rear wheels.

By ignoring the system transient characteristics, the desired target values for the sideslip angle and the yaw rate can be obtained:

$$\begin{cases} \gamma' = \frac{1}{1+AV_x^2} \cdot \frac{V_x}{l} \cdot \delta_f \\ \beta' = \frac{1 - (\frac{m}{l})(\frac{a}{bk_r})V_x^2}{1+AV_x^2} \cdot \frac{b}{l} \cdot \delta_f \end{cases} \quad (7)$$

where  $A = \frac{m}{l^2} \cdot \frac{aK_f - bK_r}{K_f K_r}$ ,  $K_f$  and  $K_r$  are the front and rear tire cornering stiffness, respectively.

Considering the above target values appear in the linear working area of the tire, the target values of the yaw rate and the sideslip angle must be limited when the tire works on the nonlinear working area [26]:

$$\begin{cases} \gamma_{\text{limit}} = \frac{0.85}{V_x} \mu g \\ \beta_{\text{limit}} = \tan^{-1}(0.02 \mu g) \end{cases} \quad (8)$$

Thus, the target values of the yaw rate and the sideslip angle obtained from the reference output level can be expressed as:

$$\begin{cases} \gamma_{-des} = \min\{|\gamma'|, \gamma_{\text{lim}}\} \cdot \text{sgn}(\delta_f) \\ \beta_{-des} = \min\{|\beta'|, \beta_{\text{lim}}\} \cdot \text{sgn}(\delta_f) \end{cases} \quad (9)$$

### 3.2. Upper Control Level

The upper control level, as shown in Figure 3, consists of speed control and yaw moment control, which generates the virtual commands of traction force and yaw moment to realize the integrated control of vehicle speed, yaw rate, and sideslip angle. Furthermore, the road adhesion coefficient is also taken into account in the yaw moment control, and the control effect becomes better.

#### 3.2.1. Speed Control

The sliding mode control is adopted in the speed control to compute the traction force required to maintain the desired longitudinal speed, as shown in Figure 3, which takes the control error of speed as the sliding surface:

$$S_{vx} = V_x - V_{x-des} \quad (10)$$

where  $V_x$  and  $V_{x-des}$  denote the actual and desired longitudinal speed, respectively. The following formula can be derived from Equation (10):

$$\dot{S}_{vx} = \dot{V}_x - \dot{V}_{x-des} = \frac{1}{m} [F_x - (F_{yfl} + F_{yfr}) \sin \delta] + V_y \cdot \gamma - \dot{V}_{x-des} \quad (11)$$

The reaching law is defined as:

$$\dot{S}_{vx} = -\varepsilon_{vx} \text{sat}(S_{vx}) - k_{vx} S_{vx} \quad (12)$$

where  $\varepsilon_{vx} > 0$ ,  $k_{vx} > 0$ , and the saturation function  $\text{sat}(S_{vx})$  can be formulated as:

$$\text{sat}(S_{vx}) = \begin{cases} \text{sgn}(x/\phi) & |s| \geq \phi \\ x/\phi & |s| < \phi \end{cases} \quad (13)$$

The longitudinal-speed control law can be finally obtained by combining Equations (11) and (12):

$$F_{x-des} = m \left[ \dot{V}_{x-des} - V_y \cdot \gamma - \varepsilon_{vx} \text{sat}(S_{vx}) - k_{vx} S_{vx} \right] + (F_{yfl} + F_{yfr}) \sin \delta \quad (14)$$

#### 3.2.2. Yaw Moment Control

The sideslip angle and the yaw rate are both selected as the control variables in the yaw moment control, as shown in Figure 3. Considering that the sideslip angle and the yaw rate are mutually coupled, and the sideslip angle is inconvenient to measure directly and its estimation accuracy is limited, the yaw moment control takes the sideslip angle as an intermediate variable in the control of the yaw rate. Based on the estimation of the sideslip angle, a fuzzy controller is developed in the yaw moment control to compute the correction factor  $K$ , so as to adjust the nominal yaw rate  $\gamma_{0m}$ , i.e.,  $\gamma_{0m} = K\gamma$ . The yaw moment is then calculated by a sliding mode controller based on the deviation of

the nominal yaw rate  $\gamma_{0m}$  from the desired yaw rate  $\gamma_{-des}$ . The structure of the yaw moment control is shown in Figure 4.

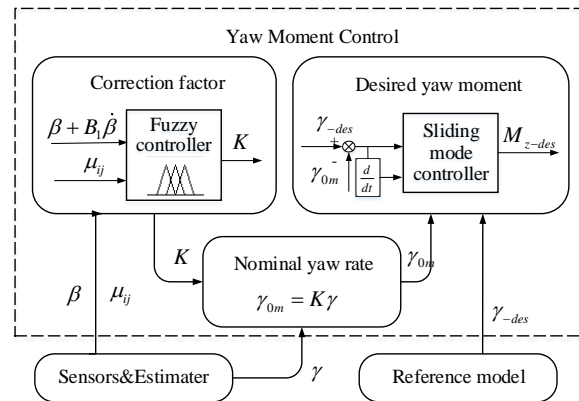


Figure 4. Structure of the yaw moment control.

Based on the phase plane method [27] and the  $\beta$ -method [28], a comprehensive control quantity, i.e.,  $\beta + B_1\dot{\beta}$ , is designed as an input of the fuzzy controller, in which the coefficient  $B_1$  reflects the influence of the rate of sideslip angle and is related to the adhesion coefficient. In addition, since the influence of the sideslip angle on the steering stability is different under different road adhesion coefficients, the adhesion coefficient  $\mu$  is also introduced into the design of the correction coefficient  $K$  as another input of the fuzzy controller. There are seven fuzzy subsets to describe the values of inputs and outputs, i.e., Positive-Big (PB), Negative-Big (NB), Positive-Medium (PM), Negative-Medium (NM), Positive-Small (PS), Negative-Small (NS), and Zero (Z). The fuzzy rules are shown in Table 1.

Table 1. Fuzzy rules of correction coefficient  $K$ .

$K$	$\beta + B_1\dot{\beta}$						
	NB	NM	NS	Z	PS	PM	PB
$\mu$	NB	PB	PB	PB	PM	PB	PB
	NM	PB	PB	PM	PM	PM	PB
	NS	PM	PM	PS	PS	PS	PM
	Z	NM	NS	NS	Z	PS	PM
	PS	NM	NM	NM	NS	NS	NM
	PM	NB	NB	NM	NM	NM	NB
	PB	NB	NB	NB	NM	NB	NB

The sliding mode controller, as shown in Figure 4, computes the yaw moment so that the nominal yaw rate  $\gamma_{0m}$  follows the desired value  $\gamma_{-des}$ . The sliding surface is defined as:

$$S_\gamma = \gamma_{0m} - \gamma_{-des} \tag{15}$$

Then the following formula can be derived from (15):

$$\dot{S}_\gamma = \dot{\gamma}_{0m} - \dot{\gamma}_{-des} = \frac{M_z}{I_z} + \frac{1}{I_z} [(F_{yfl} - F_{yfr}) \sin \delta \cdot d - (F_{yrl} + F_{yrr})b + (F_{yfr} + F_{yfl}) \cos \delta \cdot a] - \dot{\gamma}_{-des} \tag{16}$$

The reaching law is:

$$\dot{S}_\gamma = -\varepsilon_\gamma \text{sat}(S_\gamma) - k_\gamma S_\gamma \tag{17}$$

where  $\varepsilon_\gamma > 0, k_\gamma > 0$ . The yaw moment control law can be finally formulated as:

$$M_{z-des} = - (F_{yfl} - F_{yfr}) \sin \delta \cdot d + (F_{yrl} + F_{yrr})b - (F_{yfr} + F_{yfl}) \cos \delta \cdot a + I_z [\dot{\gamma}_d - \varepsilon_y \text{sat}(S_y) - k_y S_y] \tag{18}$$

### 3.3. Lower Control Level

The lower control level optimally distributes the virtual control forces generated by the upper control level, such as the traction force and the yaw moment, to each hub-motor controller in the form of the driving/brake torque commands. The relationship between the upper level and lower level can be formulated as:

$$\mathbf{v} = \mathbf{B}\mathbf{u} \quad (19)$$

where  $\mathbf{u} = [T_{fl} \ T_{fr} \ T_{rl} \ T_{rr}]^T$ ,  $\mathbf{v} = [F_{x-des} \ M_{z-des}]^T$ ,  $\mathbf{B} = \frac{1}{R} \begin{bmatrix} \cos \delta_f & \cos \delta_f & 1 & 1 \\ -d \cos \delta_f + a \sin \delta_f & d \cos \delta_f + a \sin \delta_f & -d & d \end{bmatrix}$ .

In addition to the virtual control forces from the upper control level, the torque distribution also needs to meet the friction ellipse constraint:

$$F_{xij}^2 + F_{yij}^2 \leq (\mu_{ij} F_{zij})^2 \quad (20)$$

where  $F_{zij}$  and  $\mu_{ij}$  denote the vertical load and the road adhesion coefficient at each wheel, respectively. The lateral force can be calculated from the simplified tire model.

The longitudinal force  $F_{xij}$  from the ground is related to the torque  $T_{ij}$  applied to the wheels:

$$\dot{\omega}_{ij} = \frac{1}{J_c} (T_{ij} - F_{xij}R - M_{fij}) \quad (21)$$

where  $\dot{\omega}_{ij}$ ,  $J_c$  and  $R$  denote the angular acceleration, moment of inertia and rolling radius of the wheel, respectively.  $M_{fij}$  is the rolling resistance moment.

The lower control level employs a weight-based optimal distribution algorithm in which weight factors for each tire workload usage were designed to accommodate different adhesion of each wheel.

A weight-based optimal distribution algorithm is investigated in the lower control level with the tire workload usage  $\Omega_{ij}$  as the main optimization target, which can be formulated as:

$$\Omega_{ij} = \frac{F_{xij}^2}{\mu_{ij}^2 F_{zij}^2} \quad (22)$$

The smaller the sum of tire workload usages, the greater the stability margin of the wheel, and the better the steering stability of the vehicle [17,29]. Considering that the vehicle is facing a complex road surface, the adhesion conditions at each wheel are often different. If the tire workload usages are simply added as the overall optimization target, the different adhesion conditions will be ignored. There is a possibility that the wheels in low adhesion conditions are unstable, and the wheels in the high adhesion condition still have a large stability margin. The weight factors for each tire workload usage are designed to accommodate different adhesion of each wheel as follows:

$$\psi_{ij} = \chi_{ij} \frac{\Omega_{ij}}{\sum \Omega_{ij}} \quad (23)$$

where  $\chi_{ij}$  reflects the influence of the adhesion coefficient at each wheel, the value of which is positively correlated with the adhesion coefficient.

In summary, the torque distribution algorithm of the lower control level can be described as:

$$\min J_1 = \|\Gamma \mathbf{u}\|_2 \quad (24)$$

where  $\mathbf{u} = [T_{fl} T_{fr} T_{rl} T_{rr}]^T$ ,  $\mathbf{\Gamma} = \text{diag}\left(\frac{\psi_{ij}}{\mu_{ij} F_{z_{ij} R}}\right)$ . The constraints for the torque distribution are:

$$\begin{cases} \mathbf{B}\mathbf{u} = \mathbf{v} \\ \begin{pmatrix} \mathbf{I} \\ -\mathbf{I} \end{pmatrix} \mathbf{u} \geq \begin{pmatrix} \bar{\mathbf{u}} \\ -\underline{\mathbf{u}} \end{pmatrix} \end{cases} \quad (25)$$

where  $\bar{\mathbf{u}}$  and  $\underline{\mathbf{u}}$  denote the upper and lower limits of  $\mathbf{u}$ , respectively. Considering that the intensity of the equality constraint  $\mathbf{B}\mathbf{u} = \mathbf{v}$  is too strong, it is converted to  $\min\|\mathbf{W}_v(\mathbf{B}\mathbf{u} - \mathbf{v})\|_2$  and introduced into (24) as a penalty item with a weight coefficient  $\zeta$  as follows:

$$\min J_2 = \|\mathbf{\Gamma}\mathbf{u}\|_2 + \zeta\|\mathbf{W}_v(\mathbf{B}\mathbf{u} - \mathbf{v})\|_2 \quad (26)$$

where  $\mathbf{W}_v$  denotes the distribution weight matrix, which is related to the control priority of the traction force and the yaw moment. For the low-adhesion road, the weights of the yaw moment and the traction force can be increased and reduced, respectively, so as to obtain good stability performance.

The (26) can be reformulated as:

$$J_2 = \arg \min_{\underline{\mathbf{u}} \leq \mathbf{u} \leq \bar{\mathbf{u}}} \left\| \begin{pmatrix} \zeta^{\frac{1}{2}} \mathbf{W}_v \mathbf{B} \\ \mathbf{\Gamma}_1 \end{pmatrix} \mathbf{u} - \begin{pmatrix} \zeta^{\frac{1}{2}} \mathbf{W}_v \mathbf{v} \\ 0 \end{pmatrix} \right\|_2^2 = \|\mathbf{A}\mathbf{u} - \mathbf{C}\|_2^2 \quad (27)$$

The above optimization problem can be solved by the active set method [30]. For the  $k$ th iteration, at a given  $\mathbf{u}_k$ , the correction value  $\mathbf{p}_k$  needs to be determined:

$$\begin{aligned} \min_{\mathbf{p}_k} J &= \|\mathbf{A}(\mathbf{u}_k + \mathbf{p}_k) - \mathbf{C}\|_2^2 \\ \mathbf{B}\mathbf{p}_k &= 0 \end{aligned} \quad (28)$$

If the  $\mathbf{u}_k + \mathbf{p}_k$  is a feasible solution, then  $\mathbf{u}_{k+1} = \mathbf{u}_k + \mathbf{p}_k$ , and the Lagrange multiplier  $\begin{pmatrix} \varepsilon & \lambda \end{pmatrix}^T$  can be calculated by:

$$\mathbf{A}^T(\mathbf{A}\mathbf{u}_{k+1} - \mathbf{C}) = \begin{pmatrix} \mathbf{B}^T & \mathbf{D}^T \end{pmatrix} \begin{pmatrix} \varepsilon \\ \lambda \end{pmatrix} \quad (29)$$

where  $\mathbf{D} = \begin{pmatrix} \mathbf{I} & -\mathbf{I} \end{pmatrix}^T$ . If  $\lambda \geq 0$ , then  $\mathbf{u}_{k+1}$  is the final optimal solution and the iteration ends. Otherwise, the constraint corresponding to the minimum  $\lambda$  is removed and the next iteration is performed.

If the  $\mathbf{u}_k + \mathbf{p}_k$  is not a feasible solution, then  $\mathbf{u}_{k+1} = \mathbf{u}_k + \alpha_k \mathbf{p}_k$ , and the next iteration is performed. The step  $\alpha_k$  is limited by:

$$\alpha_k = \max \left\{ \alpha_k \in [0, 1]; \underline{\mathbf{u}} \leq \mathbf{u}_k + \alpha_k \mathbf{p}_k \leq \bar{\mathbf{u}} \right\} \quad (30)$$

The iteration continues in accordance with the above steps until an optimal solution is found.

#### 4. Simulation Test and Analysis

The proposed adaptive stability control strategy was verified in a co-simulation of Carsim and Matlab/Simulink. The 4MIDEV model and driver model were developed in the Carsim, while the proposed strategy and the hub-motor model were implemented in the Simulink, as shown in the Figure 3. To further prove the improvement in steering stability, the proposed hierarchical stability control strategy, referred to as “adaptive control,” was compared with other two strategies, referred to as “common control” and “speed control”, respectively. The “common control” is proposed in [17],

in which the DYC and torque distribution algorithm didn't consider the change of the adhesion coefficient. In addition, the "speed control" has only developed a "preview-follow" driver model and a speed sliding mode controller to ensure the stability. The aforementioned stability strategies were evaluated at double-lane-change (DLC) maneuvers under the  $\mu$ -split road and joint road. The path setting for the DLC maneuver is shown in Figure 5. The parameters of the 4MIDEV and hub motors used in this study are presented in Table 2.

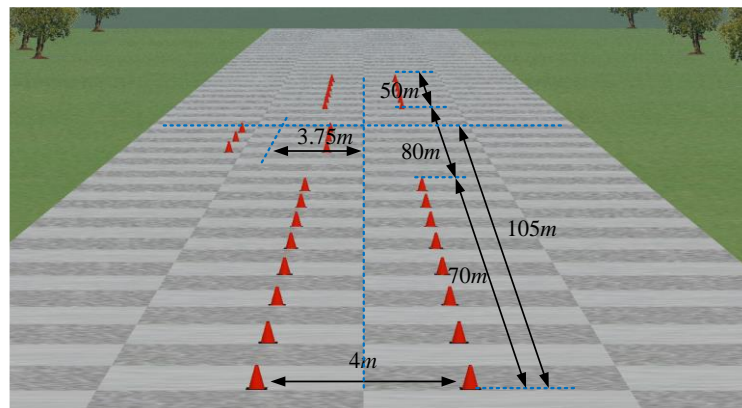


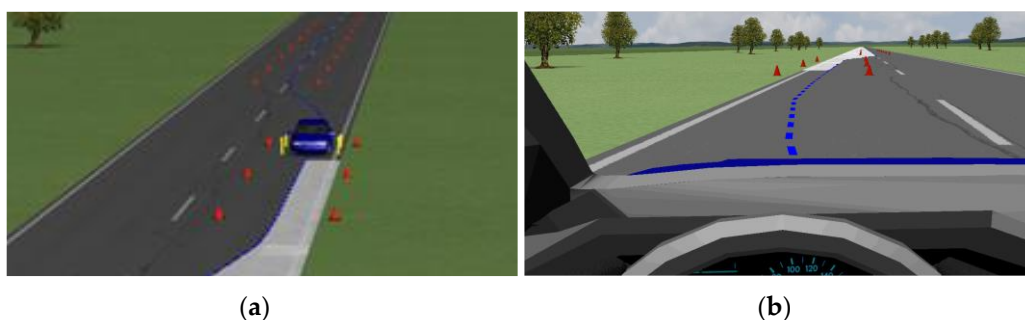
Figure 5. The path of the DLC maneuver.

Table 2. Parameters of the 4MIDEV and hub motors.

Symbol	Quantity	Value
$m$	vehicle mass	1411 kg
$I_z$	moment of inertia about the yaw axis	2031.4 kg m <sup>3</sup>
$hg$	height of the center of mass	0.54 m
$b$	length from the center of gravity (CG) to the rear wheel axis	1.56 m
$a$	length from the CG to the front wheel axis	1.04 m
$r$	tire radius	0.3 m
$d$	tread width	1.48 m
$P_m$	maximum power	28 kW
$T_m$	maximum torque	340 Nm
$n_m$	maximum speed	1200 rpm
$P_e$	rated power	14 kW
$T_e$	rated torque	170 Nm
$n_e$	rated speed	800 rpm

#### 4.1. $\mu$ -Split Road

The DLC maneuver was first conducted on the  $\mu$ -split road, as shown in Figure 6. The desired vehicle speed was set to 60 km/h and the driver's preview time was 1 s. The dynamic responses of the vehicle under different control strategies are shown in Figure 7.



(a)

(b)

Figure 6. The  $\mu$ -split road. (a) top view. (b) driver view.

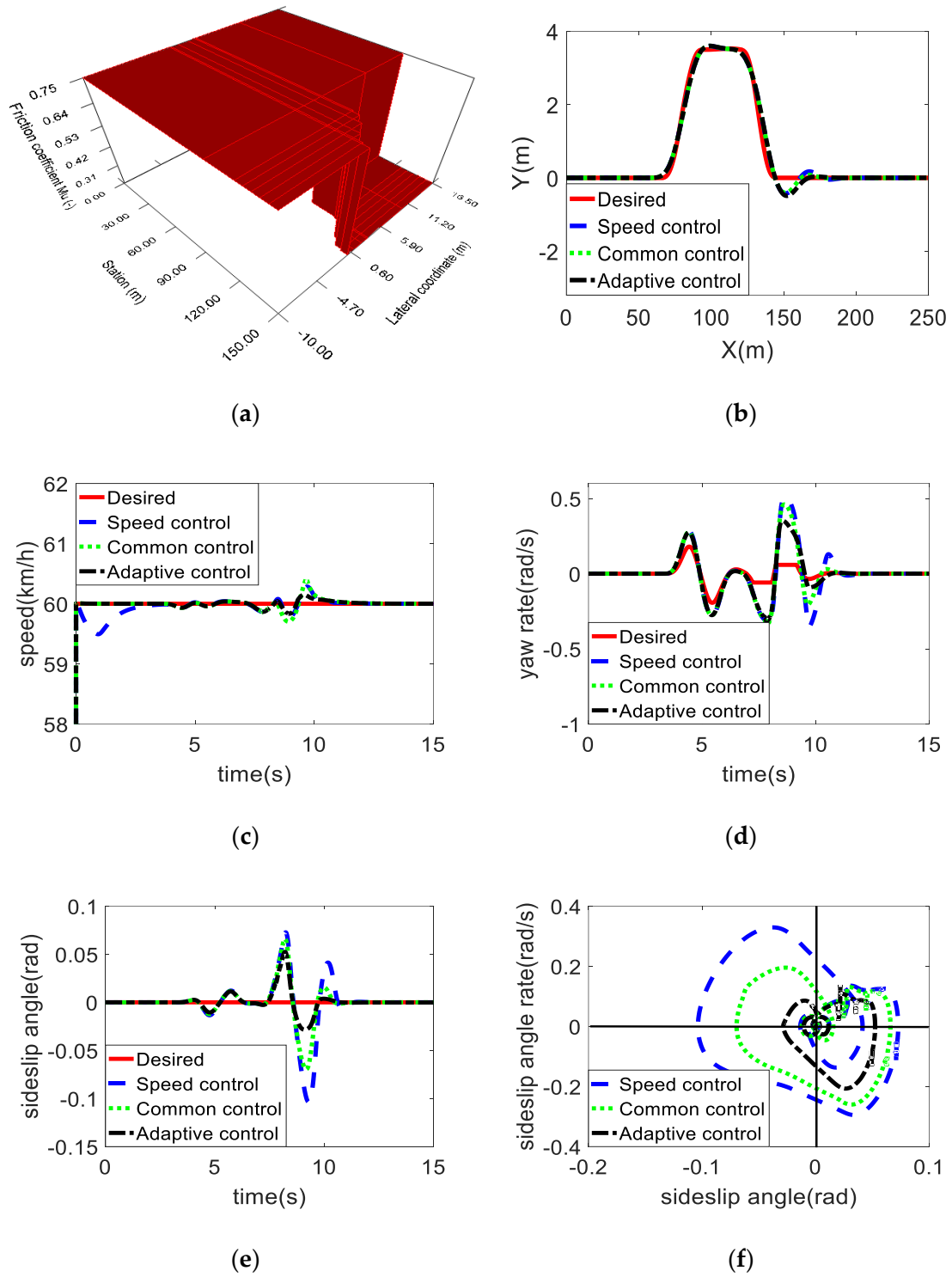
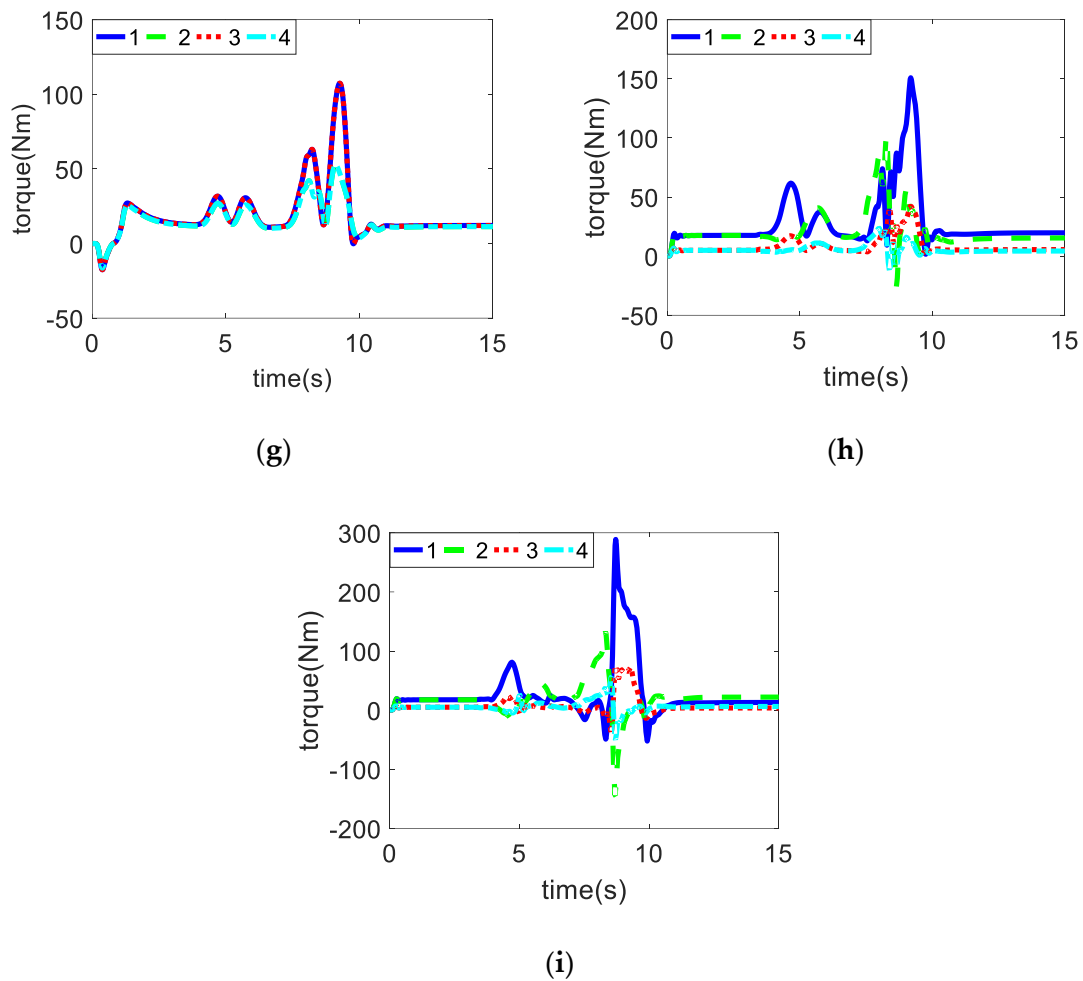


Figure 7. Cont.



**Figure 7.** Simulation results for DLC on  $\mu$ -split road ( $\mu = 0.75\text{--}0.2$ ). (a) adhesion coefficient. (b) track. (c) speed. (d) yaw rate. (e) sideslip angle. (f) phase plane. (g) torque under the speed control. (h) torque under the common control. (i) torque under the adaptive control.

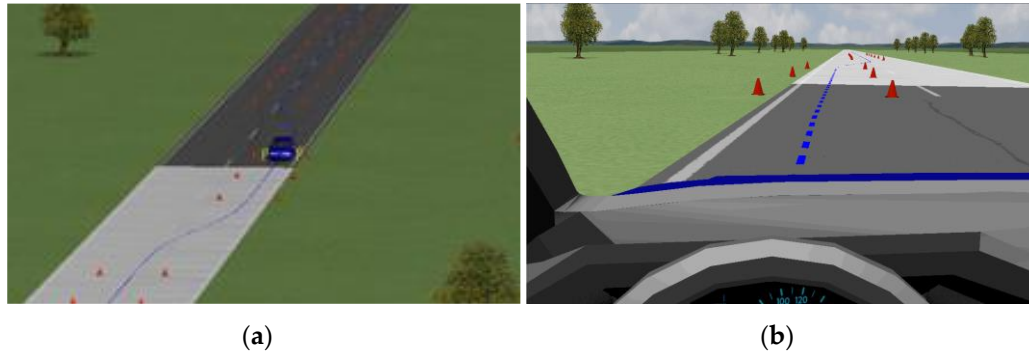
The adhesion coefficient of  $\mu$ -split road is shown in Figure 7a, which was initially set to 0.75 and suddenly became 0.75 on the half side and 0.1 on the other half side at a distance of 105 m from the starting point. Figure 7b,c show the vehicle's track and speed responses, respectively. It can be seen that the adaptive control, compared with the other two controls, performed best in achieving the following of the trajectory and speed with the smallest errors.

Figure 7d,e show the yaw rate and the sideslip angle responses of the vehicle, respectively. Both the sideslip angle and the yaw rate of aforementioned controls appeared to deviate from the desired values when the adhesion coefficient was changed, i.e., about at 7 s. However, the adaptive control could make these two quantities basically follow the desired values. The control error of the sideslip angle and the yaw rate under the adaptive control, compared with the common control, are reduced by 58.8% and 55%, respectively, which indicates that the steering stability can be ensured even in the face of varying adhesion coefficient. Figure 7f shows the sideslip angle rate and the sideslip angle in the phase plane. The curve of the adaptive control, compared with the other two controls, is most concentrated on the origin, which indicates that the stability control effect is best [21,31].

Figure 7g-i show the torque of each hub motor under the speed control, common control, and adaptive control, respectively. It can be seen that the adaptive control, compared with the other two controls, can effectively adapt to the change of the adhesion coefficient and realize different weight control of each wheel torque. For example, the output torque of the 1th and 3th wheel shown in the Figure 7i, were both increased to ensure the desired yaw moment.

4.2. Joint Road

A joint road was also developed for the DLC maneuver, as shown in Figure 8, in which the vehicle maintained a constant speed of 60 km/h. The dynamic responses of the vehicle under different stability control strategies are shown in Figure 9.



(a) (b)  
 Figure 8. The joint road. (a) top view. (b) driver view.

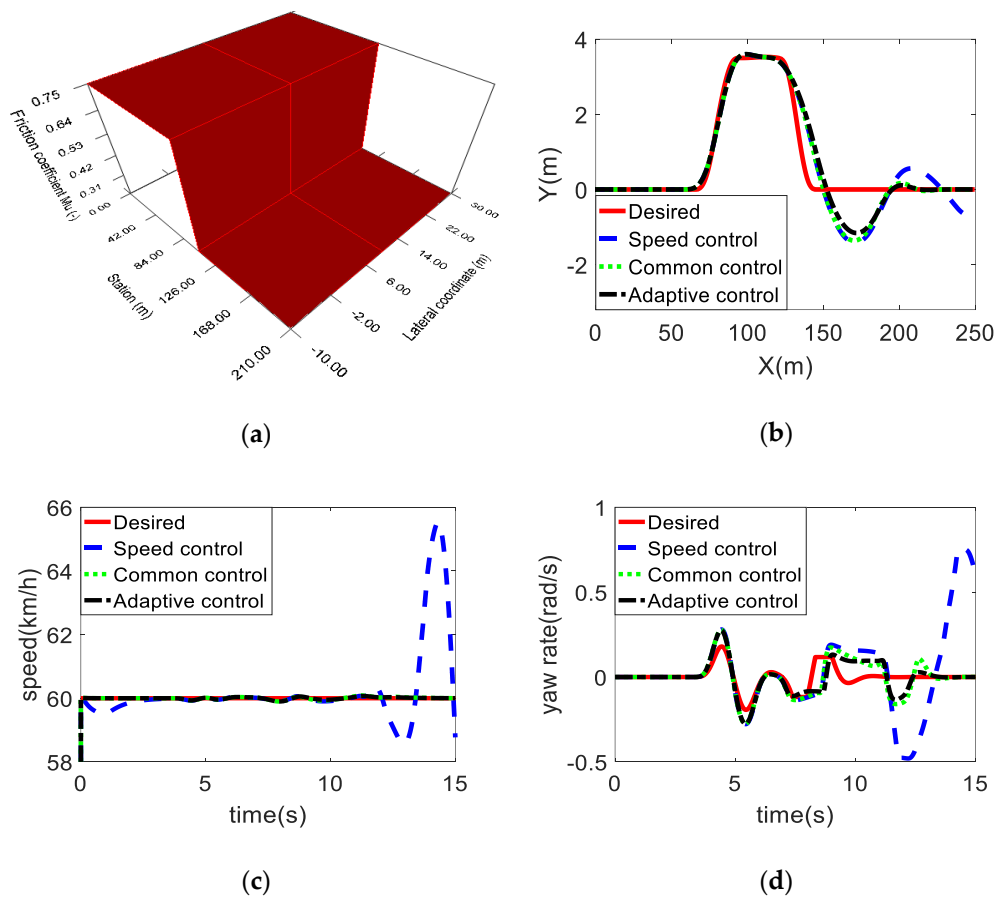
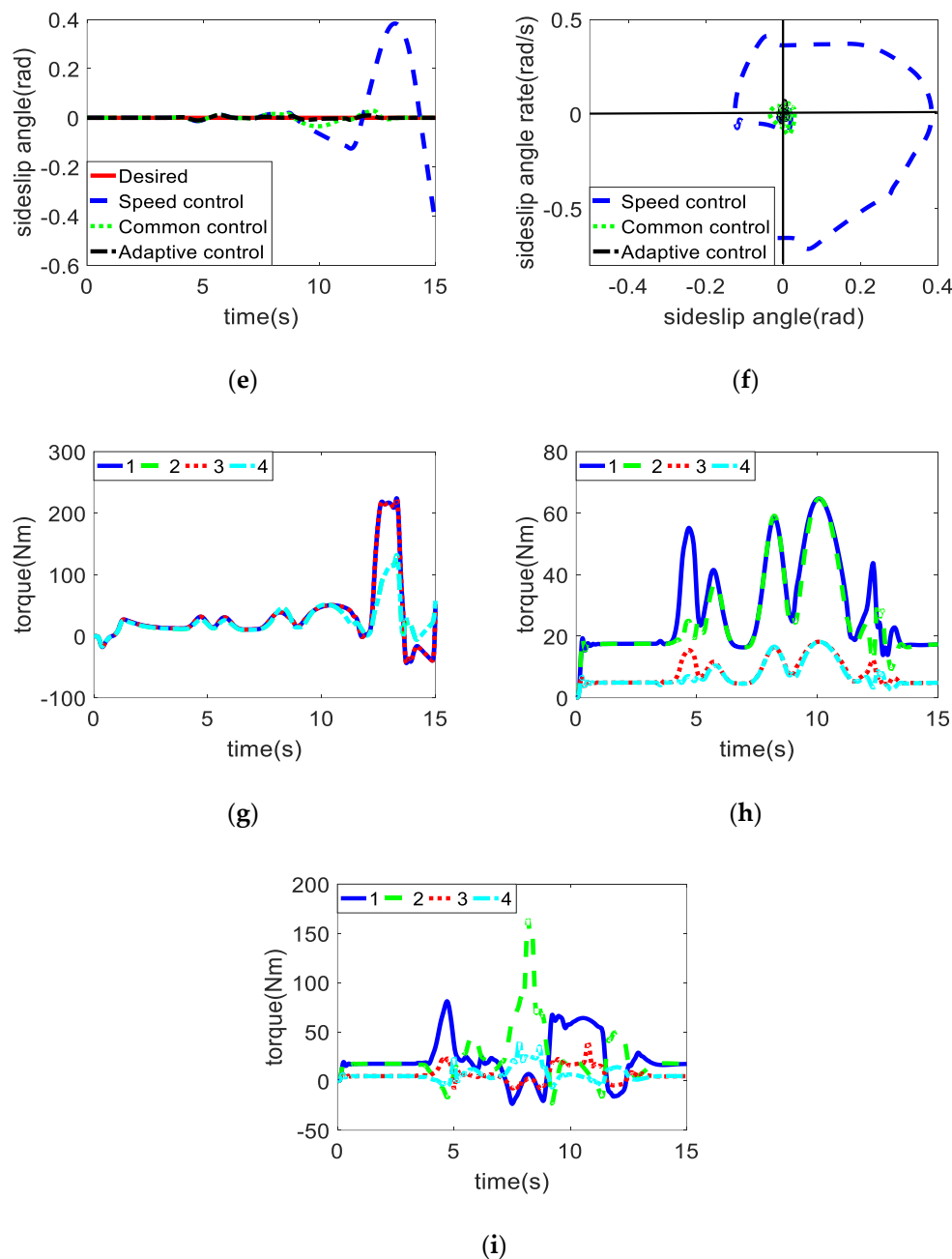


Figure 9. Cont.



**Figure 9.** Simulation results for DLC on joint road ( $\mu = 0.75\text{--}0.2$ ). (a) adhesion coefficient. (b) track. (c) speed. (d) yaw rate. (e) sideslip angle. (f) phase plane. (g) torque under the speed control. (h) torque under the common control. (i) torque under the adaptive control.

Figure 9a shows the adhesion coefficient of joint road, which was initially 0.75 and then changed to 0.2 at the middle of DLC maneuver. Figure 9b,c show the vehicle's track and speed responses, respectively. It can be seen that all the tracks of the aforementioned controls were obviously offset from the scheduled track after the change of road adhesion coefficient. In particular, the track under the speed control had a large fluctuation and tended to be unstable, whereas the adaptive control could suppress the disturbances with less deviation and fast response. In addition, both the adaptive control and the common control could basically ensure the desired speed, but the speed under the speed control was significantly deviated from the expected value.

Figure 9d,e show the yaw rate and the sideslip angle responses of the vehicle, respectively. Figure 9f shows the phase plane about the sideslip angle rate and the sideslip angle. Although

the change of the adhesion coefficient brought disturbances to the control, the adaptive control can effectively reduce the control error of the yaw rate and the sideslip angle, showing the best stability control effect. In contrast, the vehicle under the speed control was already unstable. The maximum control error of the sideslip angle and yaw rate under the common control was about 3 times and 4.1 times larger than that under the adaptive control, respectively. Furthermore, the curves of the speed control, common control, and adaptive control in the Figure 9f, tended to be more focused on the origin, which means that the stability control effect of the aforementioned controls increased gradually.

Figure 9g–i show the torque of each hub motor under the speed control, common control, and adaptive control, respectively. After the change of adhesion coefficient, the torque under speed control had an unstable oscillation, whereas the adaptive control could realize different weight control of each wheel torque, which made the 4MIDEV better adapt to changes in adhesion coefficient.

## 5. Conclusions

In order to enhance the steering stability of a four hub-motor independent-drive electric vehicle, this paper proposes a hierarchical stability control strategy that is adaptive to the road adhesion coefficient. The upper control level of the proposed strategy is composed of speed control and yaw moment control, which realizes adaptive control of the vehicle speed, yaw rate, and sideslip angle, respectively. The influences of the sideslip angle and road adhesion are both studied by fuzzy control in the yaw moment control, and the output of the DYC becomes more reasonable. The lower control level employs a weight-based optimal distribution algorithm in which weight factors for each tire workload usage are designed to accommodate different adhesion of each wheel. The different weight control of each wheel torque allows the 4MIDEV to better adapt to changes in adhesion coefficient.

The proposed stability control strategy was validated in a co-simulation using Carsim and Matlab/Simulink, in which double-lane-change maneuvers under the  $\mu$ -split road and joint road conditions were conducted. The simulation results indicate that the proposed strategy, compared with other methods, can effectively achieve robustness to changes in the adhesion coefficient and improve the steering stability of the 4MIDEV. Since the proposed method adopts sliding mode control, the chattering phenomenon is an important factor affecting the control effect. Due to the characteristics of the sliding mode control, the chattering cannot be eliminated, which may make the stability control effect become worse when the adhesion coefficient changes very rapidly and greatly. However, since the vehicle motion is slow enough compared to the sampling time, this situation hardly occurs in practice. Therefore, the good control effect of the proposed method can be basically guaranteed. In future work, the hierarchical stability control strategy will be tested through the hardware-in-the-loop test, and then the real-car test.

**Author Contributions:** Conceptualization, L.Z. and T.S.; Funding acquisition, L.Z.; Investigation, R.H.; Methodology, R.H. and T.S.; Validation, R.H.; Writing—original draft, R.H.

**Funding:** This research was funded by the National Natural Science Foundation of China, grant number 51475045.

**Conflicts of Interest:** The authors declare no conflict of interest.

## References

1. Zhang, X.D.; Göhlich, D. Integrated traction control strategy for distributed drive electric vehicles with improvement of economy and longitudinal driving stability. *Energies* **2017**, *10*, 126. [[CrossRef](#)]
2. Liu, M.C.; Gu, F.H.; Zhang, Y.Z. Ride comfort optimization of in-wheel-motor electric vehicles with in-wheel vibration absorbers. *Energies* **2017**, *10*, 1647. [[CrossRef](#)]
3. Fallah, S.; Khajepour, A.; Fidan, B.; Chen, S.K.; Litkouhi, B. Vehicle optimal torque vectoring using state-derivative feedback and linear matrix inequality. *IEEE Trans. Veh. Technol.* **2013**, *62*, 1540–1552. [[CrossRef](#)]
4. Shuai, Z.B.; Zhang, H.; Wang, J.M.; Li, J.Q.; Ouyang, M.G. Combined AFS and DYC control of four-wheel-independent-drive electric vehicles over CAN network with time-varying delays. *IEEE Trans. Veh. Technol.* **2014**, *63*, 591–602. [[CrossRef](#)]

5. Chen, Y.; Wang, J.M. Design and evaluation on electric differentials for overactuated electric ground vehicles with four independent in-wheel motors. *IEEE Trans. Veh. Technol.* **2012**, *61*, 1534–1542. [[CrossRef](#)]
6. Kim, D.H.; Kim, C.J.; Kim, S.H.; Choi, J.Y.; Han, C.S. Development of adaptive direct yaw-moment control method for electric vehicle based on identification of yaw-rate model. In Proceedings of the 2011 IEEE Intelligent Vehicles Symposium (IV), Baden-Baden, Germany, 5–9 June 2011; pp. 1098–1103.
7. Chen, J.; Yu, J.Z.; Zhang, K.X.; Ma, Y. Control of regenerative braking systems for four-wheel-independently-actuated electric vehicles. *Mechatronics* **2018**, *50*, 394–401. [[CrossRef](#)]
8. Wang, Z.P.; Wang, Y.C.; Zhang, L.; Liu, M.C. Vehicle stability enhancement through hierarchical control for a four-wheel-independently-actuated electric vehicle. *Energies* **2017**, *10*, 947. [[CrossRef](#)]
9. Ding, S.; Liu, L.; Zheng, W.X. Sliding mode direct yaw-moment control design for in-wheel electric vehicles. *IEEE Trans. Ind. Electron.* **2017**, *64*, 6752–6762. [[CrossRef](#)]
10. Ren, B.T.; Chen, H.; Zhao, H.Y.; Yuan, L. MPC-based yaw stability control in in-wheel-motored EV via active front steering and motor torque distribution. *Mechatronics* **2016**, *38*, 103–114. [[CrossRef](#)]
11. Alipour, H.; Sabahi, M.; Bannae Sharifian, M.B. Lateral stabilization of a four wheel independent drive electric vehicle on slippery roads. *Mechatronics* **2015**, *30*, 275–285. [[CrossRef](#)]
12. Zhang, X.Z.; Wei, K.X.; Yuan, X.F.; Tang, Y.Q. Optimum torque distribution for stability improvement of four-wheel distributed driven electric vehicle using coordinated control. *J. Comput. Nonlinear Dyn.* **2016**, *11*. [[CrossRef](#)]
13. Tahami, F.; Kazemi, R.; Farhanghi, S. A novel driver assist stability system for all-wheel-drive electric vehicles. *IEEE Trans. Veh. Technol.* **2003**, *52*, 683–692. [[CrossRef](#)]
14. Lin, C.; Xu, Z.F. Wheel Torque Distribution of four-wheel-drive electric vehicles based on multi-objective optimization. *Energies* **2015**, *8*, 3815–3831. [[CrossRef](#)]
15. Zou, G.C.; Luo, Y.G.; Lian, X.M.; Li, K.Q. A research of DYC for independent 4WD EV based on control target dynamic regulated. In Proceedings of the 2007 IEEE International Conference on Vehicular Electronics and Safety, Beijing, China, 13–15 December 2008; pp. 1–7.
16. Tahami, F.; Farhanghi, S.; Kazemi, R. A fuzzy logic direct yaw-moment control system for all-wheel-drive electric vehicles. *Veh. Syst. Dyn.* **2004**, *41*, 203–221. [[CrossRef](#)]
17. Zhai, L.; Sun, T.M.; Wang, J. Electronic stability control based on motor driving and braking torque distribution for a four in-wheel motor drive electric vehicle. *IEEE Trans. Veh. Technol.* **2016**, *65*, 4726–4739. [[CrossRef](#)]
18. De Novellis, L.; Sorniotti, A.; Gruber, P.; Orus, J.; Rodriguez Fortun, J.-M.; Theunissen, J.; De Smet, J. Direct yaw moment control actuated through electric drivetrains and friction brakes: Theoretical design and experimental assessment. *Mechatronics* **2015**, *26*, 1–15. [[CrossRef](#)]
19. Jin, X.J.; Yin, G.D.; Chen, N. Gain-scheduled robust control for lateral stability of four-wheel-independent-drive electric vehicles via linear parameter-varying technique. *Mechatronics* **2015**, *30*, 286–296. [[CrossRef](#)]
20. Park, J.; Park, Y. Optimal input design for fault identification of overactuated electric ground vehicles. *IEEE Trans. Veh. Technol.* **2016**, *65*, 1912–1923. [[CrossRef](#)]
21. Zhai, L.; Hou, R.F.; Sun, T.M.; Kavuma, S. Continuous steering stability control based on an energy-saving torque distribution algorithm for a four in-wheel-motor independent-drive electric vehicle. *Energies* **2018**, *11*, 350. [[CrossRef](#)]
22. Li, B.; Goodarzi, A.; Khajepour, A.; Chen, S.K.; Litkouhi, B. An optimal torque distribution control strategy for four-independent wheel drive electric vehicles. *Veh. Syst. Dyn.* **2015**, *53*, 1172–1189. [[CrossRef](#)]
23. Bakker, E.; Pacejka, H.B.; Lidne, L. A New Tire Model with an Application in Vehicle Dynamics Studies. *J. Passeng. Car.* **1989**, *98*, 101–113.
24. Li, S.Y.; Min, Y.J.; Wang, L.M.; An, L.H. Establishment and Simulation Analysis of Tire Dynamic Model. *J. Nanjing Inst. Technol. (Nat. Sci. Ed.)* **2009**, *7*, 34–38.
25. Guo, K.H.; Pan, F.; Ma, F.J. Preview optimized artificial neural network driver model. *Chin. J. Mech. Eng.* **2003**, *39*, 26–28. [[CrossRef](#)]
26. Song, P.; Tomizuka, M.; Zong, C.F. A novel integrated chassis controller for full drive-by-wire vehicles. *Veh. Syst. Dyn.* **2015**, *53*, 215–236. [[CrossRef](#)]
27. Shimada, K.; Shibahata, Y. Comparison of Three Active Chassis Control Methods for Stabilizing Yaw Moments. *J. Passeng. Car.* **1994**, *103*, 1178–1187.

28. Inagaki, S.; Kushiro, I.; Yamamoto, M. Analysis on vehicle stability in critical cornering using phase-plane method. In Proceedings of the International symposium on advanced vehicle control, Tsukuba, Japan, 24–28 October 2014.
29. Mokhiamar, O.; Abe, M. Simultaneous optimal distribution of lateral and longitudinal tire forces for the model following control. *J. Dyn. Syst. Meas. Control* **2004**, *126*, 753–763. [[CrossRef](#)]
30. Harkegard, O. Efficient active set algorithms for solving constrained least squares problems in aircraft control allocation. In Proceedings of the 41st IEEE Conference on Decision and Control, Las Vegas, NV, USA, 10–13 December 2002; pp. 1295–1300.
31. Zhang, H.; Li, X.S.; Shi, S.M.; Liu, H.F.; Guan, R.; Liu, L. Phase Plane analysis for vehicle handling and stability. *Int. J. Comput. Intell. Syst.* **2011**, *4*, 1179–1186. [[CrossRef](#)]



© 2018 by the authors. Licensee MDPI, Basel, Switzerland. This article is an open access article distributed under the terms and conditions of the Creative Commons Attribution (CC BY) license (<http://creativecommons.org/licenses/by/4.0/>).